Available online at www.sciencedirect.com

SciVerse ScienceDirect

Ceramics International 39 (2013) 5007–5012

CERAMICS INTERNATIONAL

www.elsevier.com/locate/ceramint

Synthesis, calcination and characterization of Nanosized ceria powders by self-propagating room temperature method

Branko Matović[a,*], Jelena Dukić[a], Biljana Babić[a], Dušan Bučevac[a], Zorana Dohčević-Mitrović[b], Marko Radović[b], Snežana Bošković[a]

[a]*Institute for Nuclear sciences "Vinča", Materials Science Laboratory, Belgrade University, PO Box 522, 11001 Belgrade, Serbia*
[b]*Institute of Physics, Centre for Solid State Physics and New Materials, Belgrade University, Pregrevica 118, 11080 Belgrade, Serbia*

Received 15 November 2012; received in revised form 29 November 2012; accepted 29 November 2012
Available online 7 December 2012

Abstract

Nanometric ceria powders with fluorite-type structure were obtained by applying self-propagating room temperature method. The obtained powders were subsequently thermally treated (calcined) at different temperatures for different times. Powder properties such as specific surface area, crystallite size, particle size and lattice parameter have been studied. Roentgen diffraction analysis (XRD), BET and Raman scattering measurements were used to characterize the as-obtained (uncalcined) powder as well as powders calcined at different temperatures.

It was found that the average diameter of the as-obtained crystallites is in the range of 3–5 nm whereas the specific surface area is about 70 m^2/g. The subsequent, 15 min long, calcination of as-obtained powder at different temperatures gradually increased crystallite size up to ~60 nm and reduced specific surface down to 6 m^2/g. Raman spectra of synthesized CeO_{2-y} depicts a strong red shift of active triply degenerate F_{2g} mode as well as additional peak at 600 cm^{-1}. The frequency of F_{2g} mode increased while its line width decreased with an increase in calcination temperature. Such a behavior is considered to be the result of particle size increase and agglomeration during the calcination. After the heat treatment at 800 °C crystallite size reached value larger than 50 nm. Second order Raman mode, which originates from intrinsic oxygen vacancies, disappeared after calcination.

Keywords: A. Calcination; B. X-ray methods; D. CeO_2

1. Introduction

Ceria (CeO_2) is a technologically very important material owing to its wide application as a promoter in three-way catalysts (TWCs) for the elimination of toxic auto-exhaust gases [1,2], oxygen sensor [3,4], ultraviolet absorbent [5] and glass-polishing materials [6,7]. Besides this, ceria is frequently used in fabrication of solid electrolyte for fuel cells [8–11], oxygen permeation membrane systems [12,13] and electrochromic thin-films [14–16]. It is also essential to point out an important role of ceria in the fields such as kinetics of low-temperature water–gas shift reactions [17,18], environmental chemistry and medicine [19,20]. The efficiency of the use of ceria in the above mentioned applications strongly depends on the structural features. For example, an excellent oxygen storage behavior and increased oxygen transport capacity [21,22] are the results of capability of ceria to change oxidation state in relative ease way and thus establish a balance between Ce^{+3} and Ce^{+4} anions. The change in oxidation state is followed by formation of oxygen vacancies as charge compensation defects which affects both the local structure and functionality of ceria [23]. Thus, in order to design ceria based materials with high oxygen storage and transport capacity it is essential to know how to increase the number of oxygen vacancies and to maintain a fluorite-type crystal structure at the same time. In general, there are two possibilities to obtain ceria-based oxide as an oxygen storage component. One is a promotion of Ce^{4+} reduction into Ce^{3+} [24] and the other is to chemically dope ceria with other transition or rare-earth element [25].

*Corresponding author. Tel.: +381 11 3408 753; fax: +381 11 3408 224.
E-mail address: mato@vinca.rs (B. Matović).

0272-8842/$ - see front matter © 2012 Elsevier Ltd and Techna Group S.r.l. All rights reserved.
http://dx.doi.org/10.1016/j.ceramint.2012.11.098

Another important application of ceria is its use as model material for studying plutonia properties. Ceria and plutonia have quite similar physicochemical properties such as ionic size in octahedral and cubic coordination, melting point, standard enthalpy of formation and specific heat [26,27]. Therefore, the plutonium chemistry could be well simulated using ceria instead of highly active PuO_2 [28].

Recently, much effort has been devoted to preparing CeO_2 nanoparticles and films. The methods include hydrothermal synthesis [29], sol–gel [30], homogeneous precipitation [31,32], different combustion or flame-synthesis [33–35], self propagating room temperature reaction (SPRT) [36], salt assisted aerosol decomposition [37], sonochemical and microwave heating [38], microemulsion method [39,40], gas condensation [41], and so on. Powder production method strongly affects powder properties which, in turn, affect microstructure and therefore properties of ceria ceramics [13]. For this reason a study on low-cost and time effective method is one of the main emphasis of ongoing research efforts.

In this paper ceria powders were synthesized by applying self-propagating room temperature reaction (SPRT) [42,43] in order to study behavior of nanocrystalline ceria during calcination.

2. Experimental

The ceria samples were synthesized by a SPRT method using cerium nitrate (Aldrich, USA) and NaOH (p.a. Zorka, Serbia) as starting materials. The compositions of reacting mixtures were calculated according to the nominal composition of the final reaction product. Preparation of CeO_2 powder was performed according to the following reaction:

$$2[Ce(NO_3)_3 \cdot 6H_2O] + 6NaOH + (1/2-\delta)O_2 \rightarrow 2CeO_2 + 6NaNO_3 + 9H_2O \quad (1)$$

The calculated fractions of chemicals were hand mixed in an alumina mortar with an alumina pestle for about 5 min. The reaction product mixture was rinsed in a centrifuge Centurion 1020D at 3500 rpm to remove $NaNO_3$, which was one of the reaction products [44]. Each washing run was 10 min long. This procedure was repeated three times with deionised water and two times with ethanol.

The calcination of the obtained powder at temperature ranging from 400 to 800 °C was 15 and 120 min long. All powders were characterized by means of X-ray diffraction, ellipsometry, Raman spectroscopy as well as nitrogen adsorption. Crystal structure was identified by X-ray diffraction (XRD) using filtered Cu Kα radiation (Siemens D5000). XRD was also used to evaluate the crystallite size and lattice parameters as functions of temperature. Before the measurement the angular correction was done by high quality Si standard. Lattice parameters were refined from the data using the least square procedure. Standard deviation was about 1%. Williamson-Hall plots were used to separate the effect of the size and strain in the nanocrystals, using equation:

$$\beta_{Total} \cdot \cos\theta = 0.9\lambda/D + 4\Delta d/d \cdot \sin\theta \quad (2)$$

where β_{Total} is the full width half maximum of the XRD peak, λ is the incident X-ray wave length, θ is the diffraction angle, D is crystallite size and Δd is the difference of the d spacing corresponding to a typical peak. By plotting $\beta_{Total} \cdot \cos\theta$ versus $\sin\theta$ it is possible to obtain D from the intercept and $\Delta d/d$ from the slope.

The Raman spectra were obtained using a U-1000 (Jobin-Ivon) double monochromator in back scattering geometry. The Raman spectra were excited by the 514 nm line of an Ar^+ ion laser and taken at room temperature. In order to avoid sample heating, a cylindrical focus was used and the laser power was kept bellow 10 mW.

The adsorption characteristics of the as-obtained and calcined samples were determined. Adsorption and desorption isotherms of N_2 were measured at −196 °C using the gravimetric McBain method. The specific surface area, S_{BET}, mesoporous surface area including the contribution of external surface, S_{meso}, micropore volume, V_{mic}, and pore size distribution for the powders were calculated from the isotherms. Pore size distribution was estimated by applying BJH method [45] to the desorption branch of isotherms and mesopore surface and micropore volume were estimated using the high resolution α_s plot method [45–47]. Micropore surface, S_{mic}, was calculated by subtracting S_{meso} from S_{BET}.

3. Results and discussions

Typical X-ray diffraction patterns of CeO_2 calcined at different temperatures are shown in Fig. 1. XRD analysis reveals that all peaks for each sample were significantly broadened indicating small crystallite size and/or strain. It is especially true for as-obtained powder which exhibits very

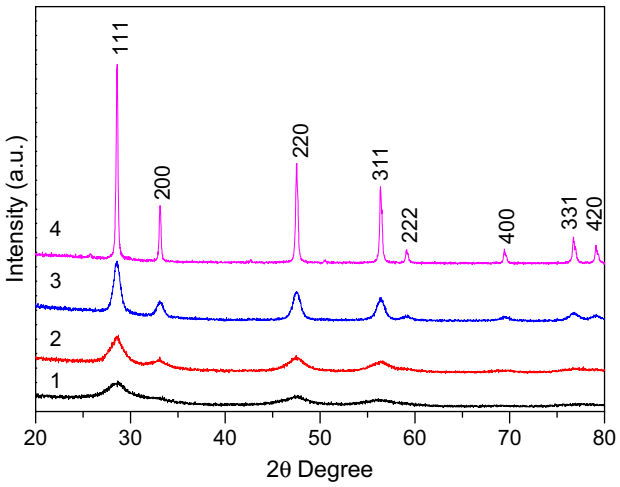

Fig. 1. Room temperature X-ray diffraction patterns of as-obtained $CeO_{2-\delta}$ samples (1) and samples calcined at 400 °C (2), 600 °C (3) and 800 °C (4) for 15 min.

diffuse diffraction lines, in such way that some atomic planes are impossible to indicate (hkl: 200, 400, 311, 420). However, the calcined powders depict somewhat sharper diffraction lines as the result of increased crystalline size. As Fig. 1 evidences, the powder calcined at 800 °C is well crystallized.

The lattice parameter, a_o (nm) and crystalline size of as-obtained as well as $CeO_{2-\delta}$ calcined at different temperatures are presented in Table 1. It was found that the lattice parameter of as-obtained powder as well as powder calcined at 400 °C is higher than the literature value for bulk material of 0.5411 nm [48,49]. This behavior can be ascribed to the existence of the microstrain fields in the crystal lattice of particles. It is believed that the fields are the most pronounced in area close to the particle surface as the concentration of surface defects such as vacancy clusters is highest. Thus, the expansion of the lattice in powders with very small particle size is due to high specific surface and consequently high concentration of oxygen vacancies associated with the presence of Ce^{3+} [50]. However, the unit cell parameter of powders calcined at 600 and 800 °C are very close to the value for cell parameter of bulk material. There are two reasons for the decrease in unit cell parameter with an increase of calcination temperature. One reason is coarsening of powder and consequent decrease in specific surface, whereas the other reason is the valance change of cerium from Ce^{3+} to Ce^{4+} due to higher thermodynamic stability of Ce^{4+} at higher temperature in ambient atmosphere. As Table 1 indicates, microstrain values are in good correlation with values of unit cell parameter and crystallite size.

Face centered cubic lattice of CeO_2 (O_h^5) allows for only one Raman active mode with F_{2g} symmetry. The Raman profile of this mode for polycrystalline sample can be expressed as Lorentzian lineshape centered at about 464 cm^{-1} [51], 465 cm^{-1} [52,53], or 466 cm^{-1} [51] with full width at half maximum (FWHM) of 9 cm^{-1} [54] or 10 cm^{-1} [55]. In CeO_2 nanocrystals, F_{2g} mode shifts to lower frequencies and deviation from the Lorentzian lineshape manifest as significant increase of F_{2g} mode FWHM and appearance of asymmetry on the lower energy side. The observed changes of F_{2g} Raman mode profile can be described successfully by taking into account the combined effects of strain and phonon confinement together with particle size distribution [56]. In $CeO_{2-\delta}$ nanocrystals, the additional mode appears at about 600 cm^{-1} which is assigned to intrinsic oxygen vacancies [57].

Table 1
Lattice parameter and crystallite size of as-obtained powder and powders calcined at different temperatures for 15 min.

Temperature (°C)	Lattice parameter (nm)	Crystallite size (nm)	Strain ($\times 10^{-3}$)
25*	0.5438	3.2	11.94(1)
400	0.5417	6.2	9.24(1)
600	0.5410	11.5	7.25(9)
800	0.5411	56.6	1.25(1)

*as-obtained (uncalcined) powder.

Fig. 2 shows the Raman spectra of samples calcined at different temperatures for 15 min and 120 min together with uncalcined sample as a reference. The F_{2g} mode for untreated sample is located at 456 cm^{-1} with FWHM of 41 cm^{-1}. Besides the main mode, the oxygen vacancy mode at 600 cm^{-1} can be clearly observed. The increase of calcination parameters (temperature and time) leads to the transformations in the Raman spectra which are characteristic for the process of crystallite size growth. In the sample calcined at 400 °C it is obvious that longer calcination time leads to the change of the F_{2g} mode bandwidth. The main F_{2g} mode at 600 °C transforms upon the calcination into Lorentzian profile whereas oxygen vacancy mode disappears from the spectrum as a consequence of improved stoichiometry.

Variation in the F_{2g} mode frequency and FWHM with crystallite size for samples calcined at different temperatures for different times is shown in Fig. 3. As the figure shows, the increase in the average crystallite size is followed by the hardening of the F_{2g} mode, i.e., shift to higher frequencies and decrease of FWHM. The most dramatic change in vibrational properties of CeO_2 nanocrystals takes place in the samples calcined at 600 °C (see Fig. 3a and b) when phonon confinement and strain effects became less dominant. At higher temperatures and prolonged time of calcination the crystallite size increases above the confinement regime causing visible variation in Raman mode profile. Finally, the frequency and FWHM of samples calcinated at 800 °C for 15 min and 120 min assume values characteristic for bulk material. Based on this, it can be concluded that most of the structural changes occur upon calcination at 600 °C. Further increase of calcination temperature does not induce significant changes in vibrational properties of CeO_2 nanocrystals. It is also worth mentioning that the change of calcination temperature has stronger influence on the vibrational properties of ceria than the calcination time.

Nitrogen adsorption isotherms, as the amount of adsorbed N_2 as a function of relative pressure at −196 °C, are shown in Fig. 4. According to the IUPAC classification [46] the isotherms are of type IV and with a hysteresis loop, which is associated with mesoporous materials. Fig. 4 shows isotherms of as-obtained powder and powders obtained after 15 min long calcinations at different temperatures. The specific surface areas calculated by BET equation, S_{BET}, are listed in Table 2. S_{BET} values, for all samples, lie within 70 and 6 $m^2\,g^{-1}$. It can be also seen that S_{BET} abruptly decreases after calcinations.

Pore size distribution (PSD) of ceria samples calcined at different temperatures is presented in Fig. 5. The figure shows that the samples are mesoporous with most of the pores radius between 2 and 4 nm. The sample calcined at 800 °C was not presented in Fig. 5 due to very low specific surface area.

α_s plots, obtained on the basis of the standard nitrogen adsorption isotherms are shown in Fig. 6. The slope of

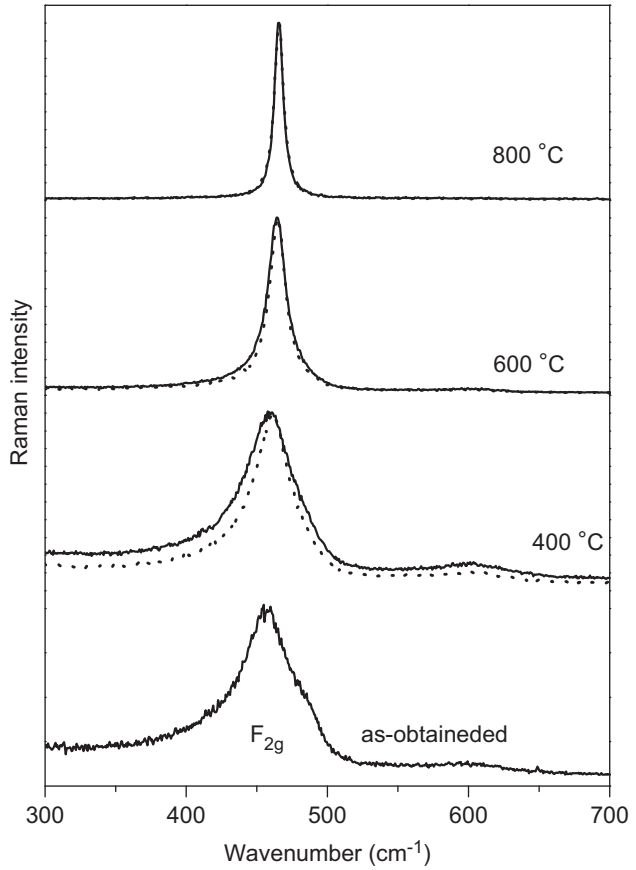

Fig. 2. Room-temperature Raman spectra of as-obtained CeO_2 nanocrystals and nanocrystals calcined at different temperatures for 15 min (solid line) and 120 min (dotted line).

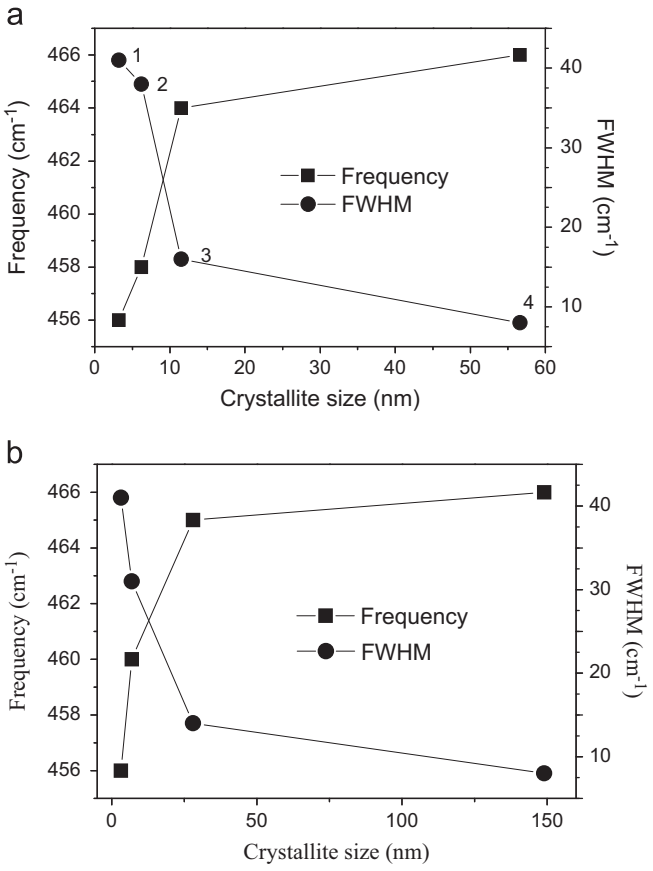

Fig. 3. Variation of the F_{2g} mode frequency and linewidth with the crystallite size for as-obtained powder and powders calcinated at different temperatures for (a) 15 min and (b) 120 min ((1) as-obtained, (2) 400 °C, (3) 600 °C, (4) 800 °C).

straight line in the medium α_s region gives a mesoporous surface area including the external surface, S_{meso}, whereas the intercept with vertical axis gives the micropore volume, V_{mic}. As mentioned before, micropore surface, S_{mic}, was calculated by subtracting S_{meso} from S_{BET}. Calculated porosity parameters (S_{meso}, S_{mic}, V_{mic}) are given in Table 2. Generally, the pore surface decreases with increasing of temperature.

According to the results given in Table 2, it can be concluded that calcination significantly changed the specific surface and porous structure of ceria powders. The higher calcinations temperature leads to decrease of specific surface and microporosity whilst the mesoporosity is almost unchanged. This behavior can be explained by the closure of small pores during the calcination as result of crystallite growth.

4. Conclusions

SPRT method was applied to produce ceria nanoparticles with an average crystalline size of 3.2 nm. They exhibited larger lattice parameter than polycrystalline material due to the presence of Ce^{3+} cations and O^{2-} vacancies. Raman spectra showed an additional mode at 600 cm^{-1}, which confirmed the presence of oxygen vacancies. Raman spectroscopy demonstrated that the increase of calcination temperature leads to the

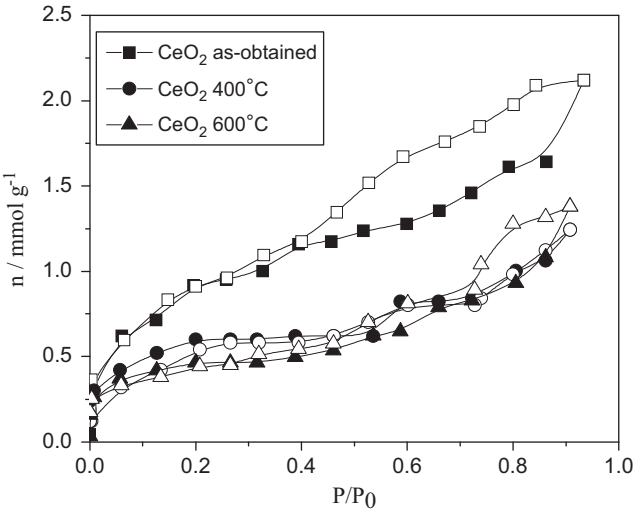

Fig. 4. Nitrogen adsorption isotherms, as the amount of N_2 adsorbed as function of relative pressure for as-obtained powder and powders calcined at 400 and 600 °C for 15 min. Solid symbols-adsorption, open symbols-desorption.

frequency shift to higher energies and to decrease of linewidth of the main F_{2g} Raman. These changes were considered to be the result of decreasing phonon confinement, strain effects and

Table 2
Porous properties of as-obtained ceria and ceria calcined at different temperatures for 15 min.

Temperature (°C)	S_{BET} (m^2/g)	S_{meso} (m^2/g)	S_{mic} (m^2/g)	V_{mic} (cm^3/g)
As-obtained	70	45	25	0.013
400	45	22	23	0.010
600	36	21	15	0.007
800	6	–	–	–

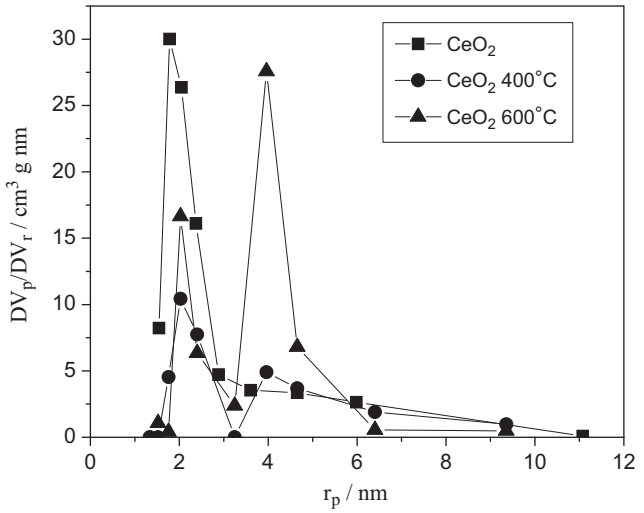

Fig. 5. Pore size distribution (PSD) for as-obtained ceria powder and powders calcined at 400 and 600 °C for 15 min.

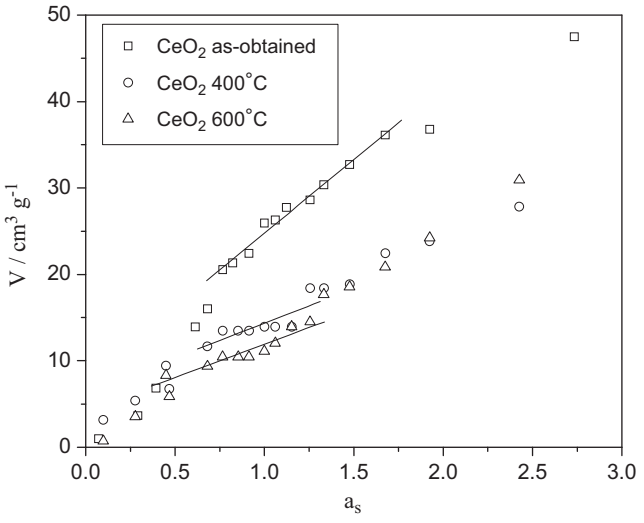

Fig. 6. α_S-plots for nitrogen adsorption isotherm of as-obtained ceria powder and powders calcined at 400 and 600 °C for 15 min.

improved stoichiometry. The second order Raman mode disappears after calcination. The specific surface area and porous structure of ceria powders considerably changed after calcination.

Acknowledgment

This project was financially supported by the Ministry of Education and Science of Serbia (Project number: III 45012).

References

[1] A. Trovarelli, Catalytic properties of ceria and CeO_2-containing materials, Catalysis Reviews: Science and Engineering 38 (1996) 439–520.
[2] J. Kaspar, P. Fornasiero, M. Graziani, Use of CeO_2-based oxides in the three-way catalysis, Catalysis Today 2 (1999) 285–298.
[3] H.J. Beie, A. Gneorich, Oxygen gas sensors based on CeO_2 thick and thin films, Sensors and Actuators, B: Chemical 4 (1991) 393–399.
[4] P. Jasinski, T. Suzuki, H.U. Anderson, Nanocrystalline undoped ceria oxygen sensor, Sensors and Actuators B: Chemical 95 (2003) 73–77.
[5] T. Morimoto, H. Tomonaga, A. Mitani, Ultraviolet ray absorbing coatings on glass for automobiles, Thin Solid Films 351 (1999) 61–65.
[6] X.D. Feng, D.C. Sayle, Z.L. Wang, M.S. Paras, B. Santora, A.C. Sutorik, T.X.T. Sayle, Y. Yang, Y. Ding, X.D. Wang, Y.S. Her, Converting ceria polyhedral nanoparticles into single crystal nanospheres, Science 312 (2006) 1504–1508.
[7] S. Armini, J. de Messemaeker, C.M. Whelan, M. Moinpour, K. Maex, Composite polymer core-ceria shell abrasive particles during oxide CMP: a defectivity study, Journal of the Electrochemical Society 155 (2008) 653–660.
[8] B.C.H. Steele, Appraisal of $Ce_{1-y}Gd_yO_{2-y/2}$ electrolytes for IT-SOFC operation at 500 °C, Solid State Ionics 129 (2000) 95–110.
[9] S.D. Park, J.M. Vohs, R.J. Gorte, Direct oxidation of hydrocarbons in a solid oxide fuel cells, Nature 404 (2000) 265–267.
[10] C.W. Sun, R. Hui, J. Roller, Cathode materials for solid oxide fuel cells: a review, Journal of Solid State Electrochemistry 14 (2010) 1125–1144.
[11] C.W. Sun, U. Stimming, Recent anode advances in solid oxide fuel cells, Journal of Power Sources 171 (2007) 247–260.
[12] O. Yildiz, G. Modolo, R. Telle, Compactibility and sintering behavior of nanocrystalline $(Th_{1-x}Ce_x)O_2$ powders synthesized by co-precipitation process, Journal of Nuclear Materials 377 (2008) 396–400.
[13] H. Yoshida, T. Inagaki, Effects of additives on the sintering properties of samaria-doped ceria, Journal of Alloys and Compounds 408–412 (2006) 632–636.
[14] I. Porqueras, C. Person, C. Corbella, M. Vives, A. Pinyol, E. Bertran, Characteristics of e-beam deposited electrochromic CeO_2 thin films, Solid State Ionics 165 (2003) 131–137.
[15] A. Azens, L. Kullman, D.D. Ragan, C.G. Granqvist, B. Hjeorvarsson, G. Vaivars, Optical and electrochemical properties of dc magnetron sputtered Ti–Ce oxide films, Applied Physics Letters 68 (1996) 3701–3703.
[16] N. Ozer, Optical properties and electrochromic characterization of sol–gel deposited ceria films, Solar Energy Materials and Solar Cells 68 (2011) 391–400.
[17] Q. Fu, A. Weber, M. Flytzani-Stephanopoulo, Nanostructured Au–CeO_2 catalysts for low-temperature water–gas shift, Catalysis Letters 77 (2001) 87–95.
[18] Q. Fu, H. Saltsburg, M. Flytzani-Stephanopoulo, Active nonmetallic Au and Pt species on ceria-based water–gas shift catalysts, Science 301 (2003) 935–938.
[19] A. Asati, S. Santra, C. Kaittanis, S. Nath, J.M. Perez, Oxidase-like activity of polymer-coated cerium oxide nanoparticles, Angewandte Chemie, International Edition 48 (2009) 2308–2312.
[20] R.W. Tarnuzzer, J. Colon, S. Patil, S. Seal, Vacancy engineered ceria nanostructures for protection from radiation-induced cellular damage, Nano Letters 5 (2005) 2573–2577.
[21] H. Inaba, H. Tagawa, Ceria-based solid electrolytes, Solid State Ionics 83 (1996) 1–16.
[22] N.Q. Minh, Ceramic Fuel Cells, Journal of the American Ceramic Society 76 (1993) 563–588.
[23] A. Trovarelli, M. Boaro, E. Rocchini, C. de Leitenburg, G. Dolcetti, Some recent developments in the characterization of ceria-based catalysts, Journal of Alloys and Compounds 323–324 (2001) 584–591.
[24] A. Gotte, K. Hermansoom, M. Baudin, Molecular dynamics simulations of reduced CeO_2: bulk and surfaces, Surface Science 552 (2004) 273–280.

[25] M. Mogenson, N.M. Sammes, G.A. Tompsett, Physical, chemical and electrochemical properties of pure and doped ceria, Solid State Ionics 129 (2000) 63–94.
[26] J.C. Marra, A.D. Cozzi, R.A. Pierce, J.M. Pareizs, A.R. Jurgensen, D.M. Missimer, in: G.L. Smith, S.K. Sundaram, D.R. Spearing (Eds.), Cerium as a Surrogate in the Plutonium Immobilized Form, in Environmental Issues and Waste Management Technologies in the Ceramic and Nuclear Industries VII, The American Ceramic Society, Westerville, Ohio, 2006.
[27] J.W. Lee, H.S. Kim, S.H. Kim, C.Y. Young, S.H. Na, G. Ledergerber, P. Heimgarbner, M. Pouchon, M. Burghartz, Preparation of simulated inert matrix fuel with different powders by dry milling method, Journal of Nuclear Materials 274 (1999) 7.
[28] C. Ganguly, in: I.J. Hasting (Ed), Second Internaional Conference on CANDU Fuel, Pembroke, Ontario, Canada, 1989, pp. 398.
[29] M. Hirano, E. Kato, Hydrothermal synthesis of nanocrystalline cerium (iv) oxide powders, Journal of the American Ceramic Society 82 (1999) 786.
[30] N.B. Kirk, J.V. Wood, The effect of the calcination process on the crystallite shape of sol–gel cerium oxide used for glass polishing, Journal of Materials Science 30 (1995) 2171–2715.
[31] P.L. Chen, I.W. Chen, Reactive cerium (IV) oxide powders by the homogeneous precipitation method, Journal of the American Ceramic Society 76 (1993) 1577–1583.
[32] B. Djuricic, S. Pickering, Nanostructured cerium oxide: preparation and properties of weakly-agglomerated powders, Journal of the European Ceramic Society 19 (1999) 1925–1934.
[33] R.D. Purohit, B.P. Sharma, K.T. Pillai, A.K. Tyagi, Ultrafine ceria powders via glycine–nitrate combustion, Materials Research Bulletin 36 (2001) 2711–2721.
[34] L. Madler, W.J. Stark, S.E. Pratsinis, Flame-made ceria nanoparticles, Journal of Materials Research 17 (2002) 1356–1362.
[35] S. Bošković, S. Zec, B. Matović, M. Zinkevich, F. Aldinger, Doped and co-doped CeO_2: preparation and properties, Ceramics International 34 (2008) 2001–2006.
[36] B. Matović, Z. Dohčević-Mitrović, M. Radović, Z. Branković, G. Branković, S. Bošković, Z. Popović, Synthesis and characterization of ceria based nanometric powders, Journal of Power Sources 193 (2009) 146–149.
[37] B. Xia, I.W. Lenggoro, K. Okuyama, Synthesis of CeO_2 nanoparticles by salt-assisted ultrasonic aerosol decomposition, Journal of Materials Chemistry 11 (2001) 2925–2927.
[38] H. Wang, J.J. Zhu, J.M. Zhu, X.H. Liao, S. Xu, T. Ding, H.Y. Chen, Preparation of nanocrystalline ceria particles by sonochemical and microwave assisted heating methods, Physical Chemistry Chemical Physics 4 (2002) 3794–3799.
[39] T. Masui, K. Fujiwara, K. Machida, G. Adachi, T. Sakata, H. Mori, Characterization of cerium (IV) oxide ultrafine particles prepared using reversed micelles, Chemistry of Materials 9 (1997) 2197–2204.
[40] Y.J. He, B.L. Yang, G.X. Cheng, Controlled synthesis of CeO_2 nanoparticles from the coupling route of homogenous precipitation with microemulsion, Materials Letters 57 (2003) 1880–1884.
[41] N. Guillou, L.C. Nistor, H. Fuess, H. Hahn, Microstructural studies of nanocrystalline CeO_2 produced by gas condensation, Nanostructured Materials 8 (1997) 545–557.
[42] S. Bošković, D. Djurović, Z. Dohčević-Mitrović, Z. Popović, M. Zinkevich, F. Aldinger, Self-propagating room temperature synthesis of nanopowders for solid oxide fuel cells (SOFC), Journal of Power Sources 145 (2005) 237–242.
[43] S. Bošković, S. Zec, M. Ninić, J. Dukić, B. Matović, D. Djurović, F. Aldinger, Nanosized ceria solid solutions obtained by different chemical routes, Journal of Optoelectronics and Advanced Materials 10 (2008) 515–519.
[44] S. Bošković, D. Djurović, B. Matović, M. Čančarević, Z. Mitrović-Dohčević, Z. Popović, M. Zinkevich, F. Aldinger, Reaction of $Ce_{1-x}Re_xO_{2-\delta}$ nanopowders synthesis, Materials Science Forum 518 (2006) 95–100.
[45] E.P. Barrett, L.G. Joyner, P.P. Halenda, The determination of pore volume and area distributions in porous substances. Computations from nitrogen isotherms, Journal of the American Chemical Society 73 (1951) 373–380.
[46] K. Kaneko, C. Ishii, M. Ruike, H. Kuwabara, Origin of superhigh surface area and microcrystalline graphitic structures of activated carbons, Carbon 30 (1992) 1075.
[47] M. Kruk, M. Jaroniec, K.P. Gadakaree, Nitrogen adsorption studies of novel synthetic active carbons, Journal of Colloid and Interface Science 192 (1997) 250–256.
[48] X.D. Liu, H.Y. Zhang, K. Lu, Z.Q. Hu, The lattice expansion in nanometer-sized Ni polycrystals, Journal of Physics: Condensed Matter 6 (1994) L497–L502.
[49] Y.H. Zhao, K. Zhang, K. Lu, Grain-size dependence of thermal properties of nanocrystalline element selenium studied by X-ray diffraction, Physical Review B 56 (1997) 14322.
[50] W. Qin, Z.H. Chen, P.Y. Huang, Y.H. Zhuang, Crystal lattice expansion of nanocrystalline materials, Journal of Alloys and Compounds 292 (1999) 230–232.
[51] J.E. Spanier, R.D. Robinson, F. Zhang, S.W. Chan, I.P. Herman, Size-dependent properties of CeO_{2-y} nanoparticles as studied by Raman scattering, Physical Review B 64 (2001) 245407.
[52] V.G. Keramidas, W.B. White, Raman spectra of oxides with the fluorite structure, Journal of Chemical Physics 59 (1973) 1561–1562.
[53] G.A. Kourouklis, A. Jayaraman, G.P. Espinosa, High-pressure Raman study of CeO_2 to 35 GPa and pressure-induced phase transformation from the fluorite structure, Physical Review B 37 (1988) 4250–4253.
[54] Igor Kosacki, Vladimir Petrovsky, U. Anderson, Philippe Colomban, Raman spectroscopy of nanocrystalline ceria and zirconia thin films, Journal of the American Ceramic Society 85 (2002) 2646–2650.
[55] W.H. Weber, K.C. Hass, J.R. McBride, Raman study of CeO_2: second-order scattering, lattice dynamics, and particle-size effects, Physical Review B 48 (1993) 178–185.
[56] Z.D. Dohčević-Mitrović, M.J. Šćepanović, M.U. Grujić-Brojčin, Z.V. Popović, S.B. Bošković, B.M. Matović, M.V. Zinkevich, F. Aldinger, The size and strain effects on the Raman spectra of $Ce_{1-x}Nd_xO_{2-d}$ (0ÈxÈ0.25) nanopowders, Solid State Communications 137 (2006) 387–390.
[57] J.R. McBride, K.C. Hass, B.D. Poindexter, W.H. Weber, Raman and Xray studies of $Ce_{1-x}RE_xO_{2-y}$, where RE=La, Pr, Nd, Eu, Gd, and Tb, Journal of Applied Physics 76 (1994) 2435.